

ELECTRONIC SUPPLEMENTARY INFORMATION

Neodymium δ -diketonate showing slow magnetic relaxation and acting as ratiometric thermometer based on near-infrared emission

Kunal Kumar,^a Daisuke Abe,^a Keiko Komori-Orisaku,^a Olaf Stefańczyk,^a Koji Nakabayashi,^a Julia R. Shakirova,^b Sergey P. Tunik^b and Shin-ichi Ohkoshi*^a

^a Department of Chemistry, School of Science, The University of Tokyo, 7–3–1 Hongo, Bunkyo-ku, Tokyo 113–0033, Japan

^b Institute of Chemistry, St.-Petersburg State University, 26 Universitetskiy pr., Peterhof, St.-Petersburg, Russia

*Corresponding author: ohkoshi@chem.s.u-tokyo.ac.jp

LIST OF CONTENTS

Figure S1. Infrared absorption (IR) spectra measured in KBr for A and B , and compared with IR signals of 4,4,4-trifluoro-1-(2-thienyl)-1,3-butanedione (TTA), 4,4'-azopyridine (Azo-py,) and 4-hydroxypyridine (4-pyOH).....	3
Figure S2. Thermogravimetric analyses for A (a) and B (b)	4
Comment to thermogravimetric analyses	4
Figure S3. IR Spectrum of A at 300 K compared with Azopy, TTA and nujol, and temperature dependent IR spectrum of A	5
Comment to Temperature Dependent IR Spectrum.	6
Table S1. Crystal data and structure refinement parameters for A and B	7
Figure S4. The asymmetric unit of A and B with atom labelling.....	8
Figure S5. Detailed views of the crystal structure of A	8
Figure S6. Detailed views of the crystal structure of B	9
Table S2. Detailed structural parameters of A and B	10
Table S3. Results of Continuous Shape Measure (CSM) analyses for $[Nd^{III}(TTA)_3(CH_3OH)_2]$ structural units in the crystal structures of A	10
Figure S7. Experimental powder X-ray diffraction patterns of A and B compared with simulated ones for single crystal structures	11

Comment to powder X-ray diffraction patterns.	11
Figure S8. Room temperature solid-state UV–Vis–NIR absorption (Kubelka–Munk function) spectra of A compared with relevant spectra of Azo-py and TTA.	12
Figure S9. Room temperature solid-state UV–Vis–NIR absorption (Kubelka–Munk function) spectrum of A overlapped with spectra of Azo-py and TTA as well as B overlapped with spectra of 4-pyOH and TTA.	14
Figure S10. Temperature dependent UV–Vis–NIR absorption (Kubelka–Munk function) spectra of A	15
Figure S11. Comparison of emission and excitation spectra of A and B for the excitation wavelength of 392 nm at the indicated temperatures.	15
Figure S12. Solid state NIR emission measured for the temperature ranging from 10 - 370 K for the excitation wavelength of 360 nm in the heating and cooling cycle (a), the related excitation spectra of A measured at relevant emission wavelength of 895 nm (b) for shown temperatures and the emission peak at 895 nm measured at various temperature for excitation wavelength of 360 nm (c). Part (d) and (e) presents temperature dependences of relative thermal sensitivity, S_r , of compound A computed from the $\Delta(T)$ calibration curves for two investigated excitation wavelengths of 360 and 392 nm, respectively.....	16
Figure S13. The temperature dependences of the temperature uncertainty, δT , calculated using the experimental relative errors of thermometric parameters, Δ for A	17
Figure S14. Stimulated UV–Vis–NIR absorption spectra of TTA and A in 200 – 1000 nm range using Gaussian 09 software and compared with experimental result.	17
Comments on UV-VIS-NIR absorption spectra.	17
Figure S15. The temperature dependence of absolute intensity of the peak centred around 360 nm and 392 nm in the excitation spectra of A for the emission wavelength of 1056 nm, thermal dependent intensity ratio of corresponding peak at 360 and 392 nm in the excitation spectra of A and temperature dependence of absolute emission intensity peaked at 1056 nm for excitation light of 392 nm for complex A	18
Figure S16. Trend of thermometric parameter, Δ for A under the excitation by 392 nm and 360 nm light during temperature cycling between 200 and 50 K showing nice repeatability for both excitation wavelengths.	19
Figure S17. The <i>dc</i> magnetic properties: (a) temperature dependences of product molar magnetic susceptibility and temperature ($\chi_M T$) in $H_{dc} = 1$ kOe for A and (b) magnetic field dependences of magnetization at $T = 1.85$ K for A	20
Debye model for single relaxation process	20
Figure S18. Frequency dependencies of out-of-plane χ_M'' magnetic susceptibility of A in <i>ac</i> magnetic field of 3 Oe at $T = 1.85$ K in various indicated <i>dc</i> magnetic fields.	21
Figure S19. The <i>ac</i> magnetic characteristics of the A in $H_{dc} = 1000$ Oe and $H_{ac} = 3$ Oe: frequency (ν) dependences of the in-plane χ_M' (a) and the related $\chi_M''-\chi_M'$ Argand plots (b).	21
Table S5. Parameters obtained by fitting the Argand $\chi_M''-\chi_M'$ plots ($H_{dc} = 1000$ Oe, Figure 9) of A using the generalized Debye model.	22
Figure S20. The <i>ac</i> magnetic characteristics of sample A after heating at 360 K in $H_{dc} = 1000$ Oe and $H_{ac} = 3$ Oe: frequency (ν) dependences of the in-plane χ_M' (a) and the related $\chi_M''-\chi_M'$ Argand plots (b), frequency (ν) dependences out-of-plane, χ_M'' (c) components of the complex magnetic susceptibility for the indicated temperatures of the 1.85–7.0 K range and the temperature dependence of relaxation times (τ) presented as $\ln(\tau)$ versus T^{-1} plots (d).	23
Table S6. The outline of Nd ^{III} complexes revealing single-molecule magnet behaviour.	24
References to Supporting Information	25

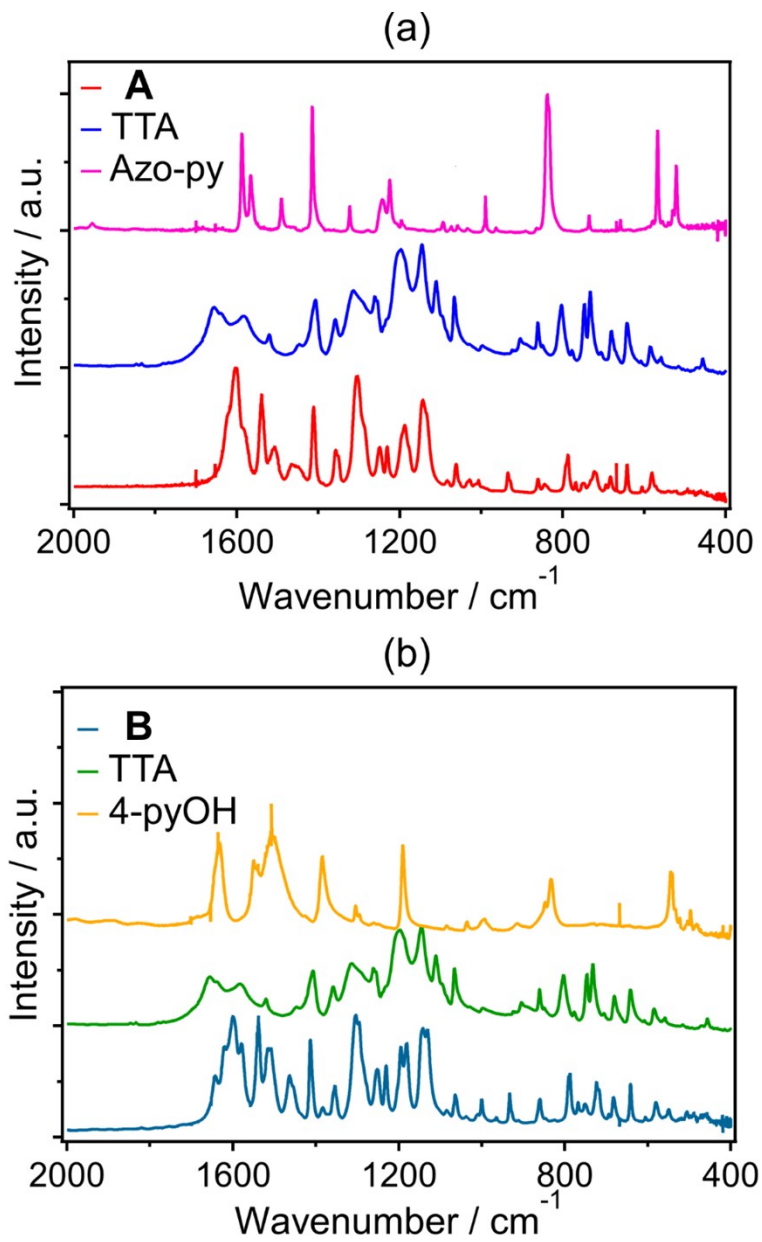


Figure S1. Infrared absorption (IR) spectra measured in KBr for **A** (a) and **B** (b), and compared with IR signals of 4,4,4-trifluoro-1-(2-thienyl)-1,3-butanedione (TTA), 4,4'-azopyridine (Azo-py,) and 4-hydroxypyridine (4-pyOH).

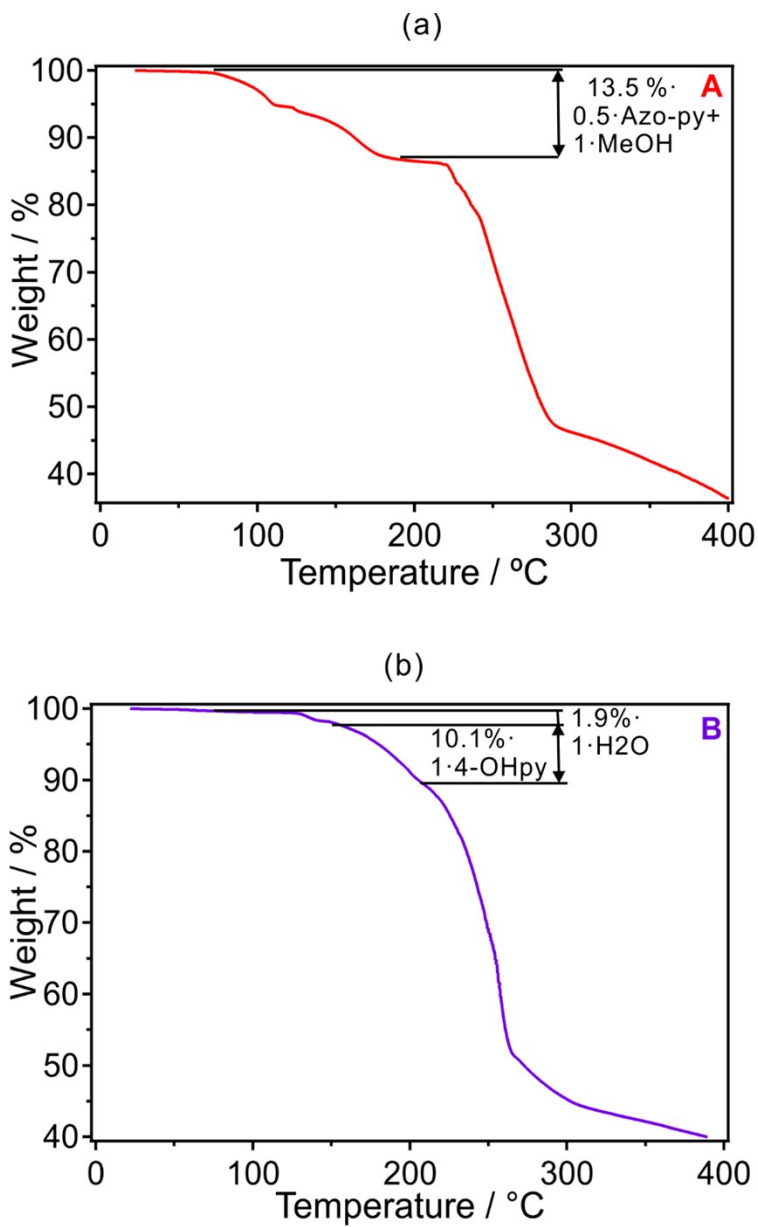


Figure S2. Thermogravimetric analyses for **A** (a) and **B** (b) .

Comment to thermogravimetric analyses

TGA curves for **A** and **B** vary significantly among themselves due to the presence of various ligands (methanol and Azo-py for **A**, and water and 4-OHpy for **B**) and a different composition (**Figure S2**). In the first step, assembly **A** loses 6.0% of its initial mass due to removal of two equivalent of co-ordinated methanol around 100 °C. The broad plateau is visible until 160 °C followed by decomposition of 4-Azopy at 210 °C which gives sharp weight loss by 2.6% which might be assigned to the prior removal N₂ molecule from 4-Azopy. Further increase of

temperature above 210°C leads to release of half equivalent of 4-Azopy and partial decomposition of coordinated TTA anion, due to which the mass decreased by 36 % at 275°C. Finally, augmentation of temperature up to 375°C results in the weight decrease down to 45% of initial one, however, even at this temperature **A** still contains TTA molecules or products of their decomposition. In case of product **B**, the first coordinated water molecule is released at around 150°C and it is related to the weight loss of 1.9%. Further heating up to 220°C induces the removal of 4-OHpy which corresponds to the 10.1% of mass loss. Next increase of temperature up to 260°C initiate thermal decomposition of TTA in **B**, however, remains of TTA can be detected even at 400°C.

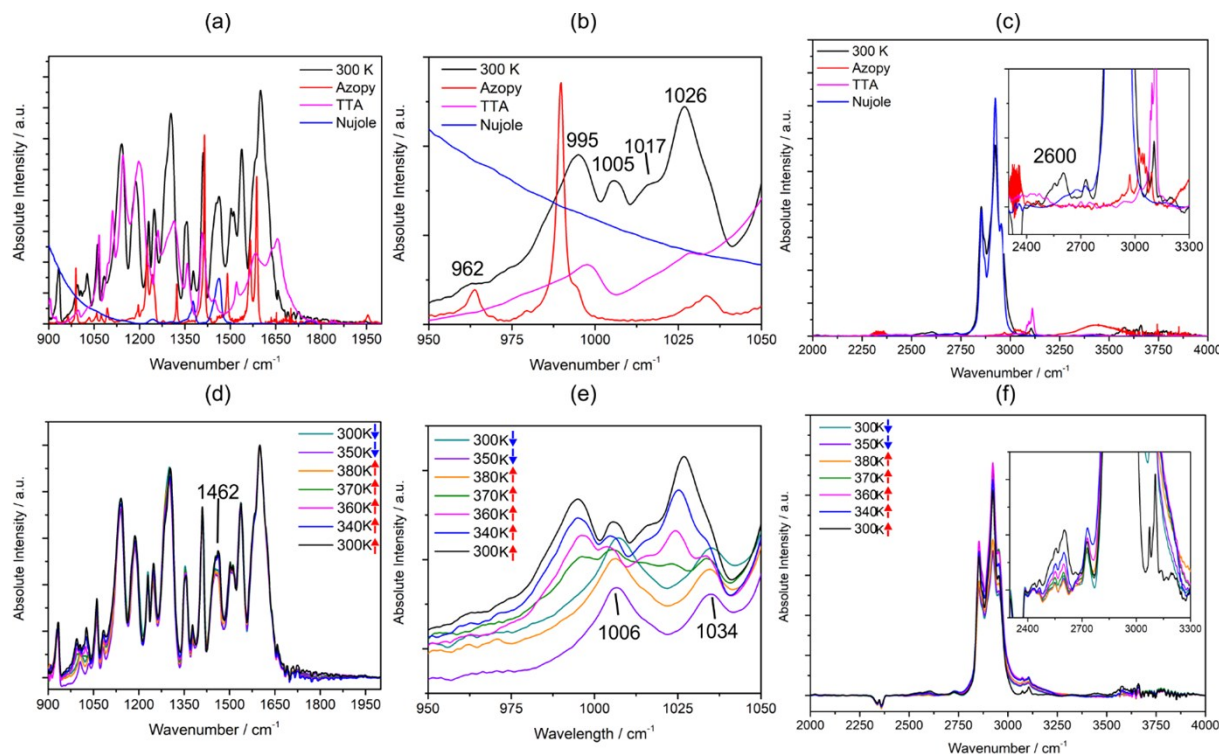


Figure S3. IR Spectrum of **A** at 300 K compared with Azopy, TTA and nujol as references in the wavenumber range of 900 – 2000 cm⁻¹ (a), 950 – 1050 cm⁻¹ (b) and 2000 – 4000 cm⁻¹ (c, along with enlarged view in the wavenumber range of 2300 – 3300 cm⁻¹). Corresponding to the same wavenumber region with respect to the above set of three spectra, temperature dependent IR spectrum of **A** has been shown in (d), (e) and (f) for the indicated heating (300 – 380 K) and cooling (350 and 300 K) temperatures.

Comment to Temperature Dependent IR Spectrum.

In order to supplement the TGA data, we analysed the thermal dependence IR spectra of **A**. Using the overlapped spectra of **A**, Azopy, TTA and nujol, the peaks corresponding to C-O (single bond) and C-H bond frequency were identified (as shown in part (b) and enlarged (c)). In the first part of spectrum ($900 - 2000 \text{ cm}^{-1}$) changes can be clearly seen in the $950 - 1050 \text{ cm}^{-1}$ range. As we increase the temperature peak intensity near 995, 1005, 1017 and 1026 nm decreases until 370 K resulting into two broad peaks centred around 1006 nm and 1034 nm. Systematic decrease in intensity and disappearance of peaks near 995 and 1026 nm indicated that these two peaks correspond C-O single bond frequency, and remaining two peaks are related to the combined contribution from the Azopy and TTA.^{S1} Additionally, peaks around 2600 cm^{-1} with several shoulders belongs to C-H bond vibration, intensity of these peaks decreases upon increasing the temperature indicating the decrease in the C-H bonds population confirming the release of methanol.^{S1}

Table S1. Crystal data and structure refinement parameters for **A** and **B**.

Compound	A (Azo-py)	A (heated)	B (4-OHpy)
Formula	C ₃₁ H ₂₄ F ₉ N ₂ NdO ₈ S ₃	C ₃₁ H ₂₄ F ₉ N ₂ NdO ₈ S ₃	C ₂₉ H ₁₈ F ₉ NNdO ₈ S ₃
Formula weight [g·mol ⁻¹]	963.94	963.94	919.86
T [K]	90.15	340.15	296 (2)
λ [Å]	0.71075 (Mo Kα)	0.71075 (Mo Kα)	0.71075 (Mo Kα)
Crystal system	monoclinic	monoclinic	triclinic
Space group	P2 ₁ /n	P2 ₁ /n	P-1
Unit cell	<i>a</i>	10.9488(12)	10.8784(4)
	<i>b</i>	18.0795(17)	18.8797(8)
	<i>c</i>	19.0595(18)	19.2659(7)
	α	90	90
	β	106.326(8)	105.874(8)
	γ	90	81.211(6)
<i>V</i> [Å ³]	3620.7(6)	3805.9(3)	1617.09(11)
<i>Z</i>	4	4	2
Calcd. density [g·cm ⁻³]	1.768	1.682	1.889
Absorption coefficient [mm ⁻¹]	1.705	1.622	1.903
<i>F</i> (000)	1908	1908	904.0
Crystal size [mm ³]	0.264 × 0.229 × 0.106	0.383 × 0.200 × 0.130	0.220 × 0.190 × 0.09
2θ range [deg]	6.338-52.72	3.912-50.056	6.282-54.972
Limiting indices	-13 < <i>h</i> < 13	-12 < <i>h</i> < 12	-12 < <i>h</i> < 13
	-22 < <i>k</i> < 22	-22 < <i>k</i> < 22	-14 < <i>k</i> < 16
	-23 < <i>l</i> < 23	-22 < <i>l</i> < 22	-17 < <i>l</i> < 17
Collected refls	46529	271216	15634
Unique refls	7324	6561	7353
<i>R</i> _{int}	0.0477	0.0814	0.0319
Completeness [%]	99.0	97.8	99.2
Data/ restraints/ parameters	7324/112/586	6561/142/579	7353/7/485
GOF on <i>F</i> ²	1.483	1.169	1.076
Final R indices	<i>R</i> ₁ = 0.0698 [<i>I</i> > 2σ(<i>I</i>)] <i>wR</i> ₂ = 0.1089 [<i>I</i> > 2σ(<i>I</i>)]	<i>R</i> ₁ = 0.0849 [<i>I</i> > 2σ(<i>I</i>)] <i>wR</i> ₂ = 0.1313 [<i>I</i> > 2σ(<i>I</i>)]	<i>R</i> ₁ = 0.0326 [<i>I</i> > 2σ(<i>I</i>)] <i>wR</i> ₂ = 0.0742 [<i>I</i> > 2σ(<i>I</i>)]
	<i>R</i> ₁ = 0.0746 (all data) <i>wR</i> ₂ = 0.1101 (all data)	<i>R</i> ₁ = 0.1185 (all data) <i>wR</i> ₂ = 0.1423 (all data)	<i>R</i> ₁ = 0.0402 (all data) <i>wR</i> ₂ = 0.0765 (all data)
Largest diff peak/hole	1.29/-3.063	0.82/-1.512	1.846/-0.818

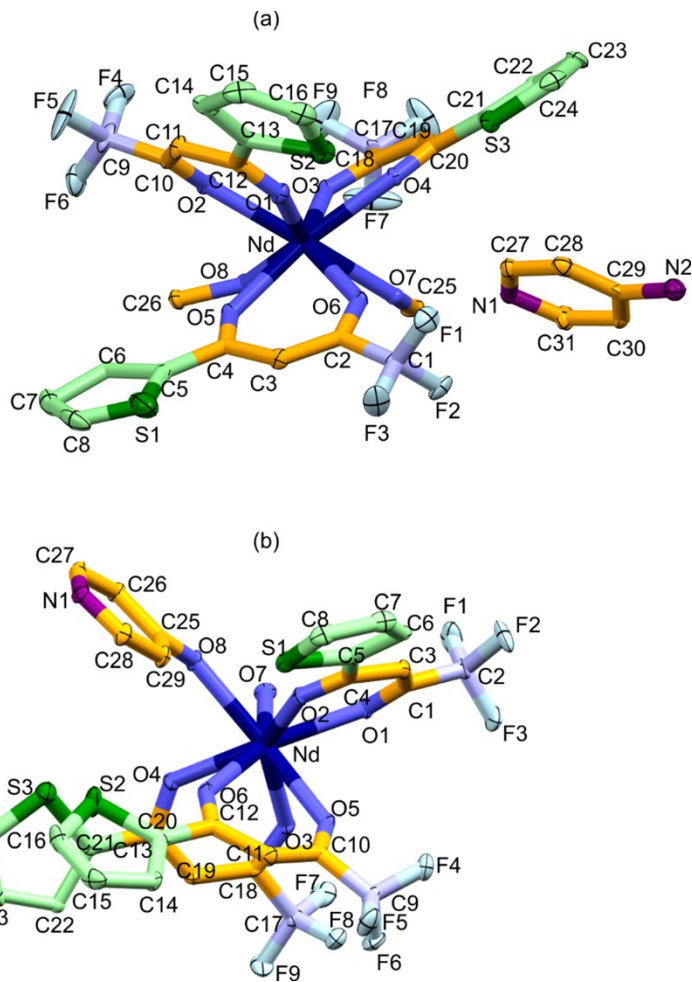


Figure S4. The asymmetric unit of **A** and **B** with atom labelling.

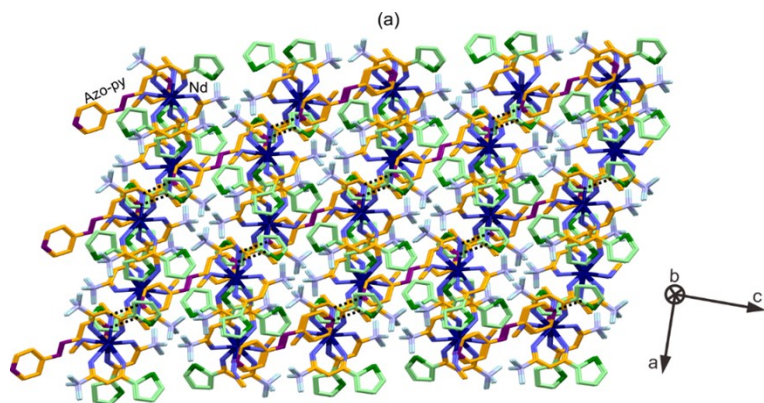


Figure S5. Detailed views of the crystal structure of **A**: (a) the view along tilted *b*-axis with indicated hydrogen bonding by black dotted lines.

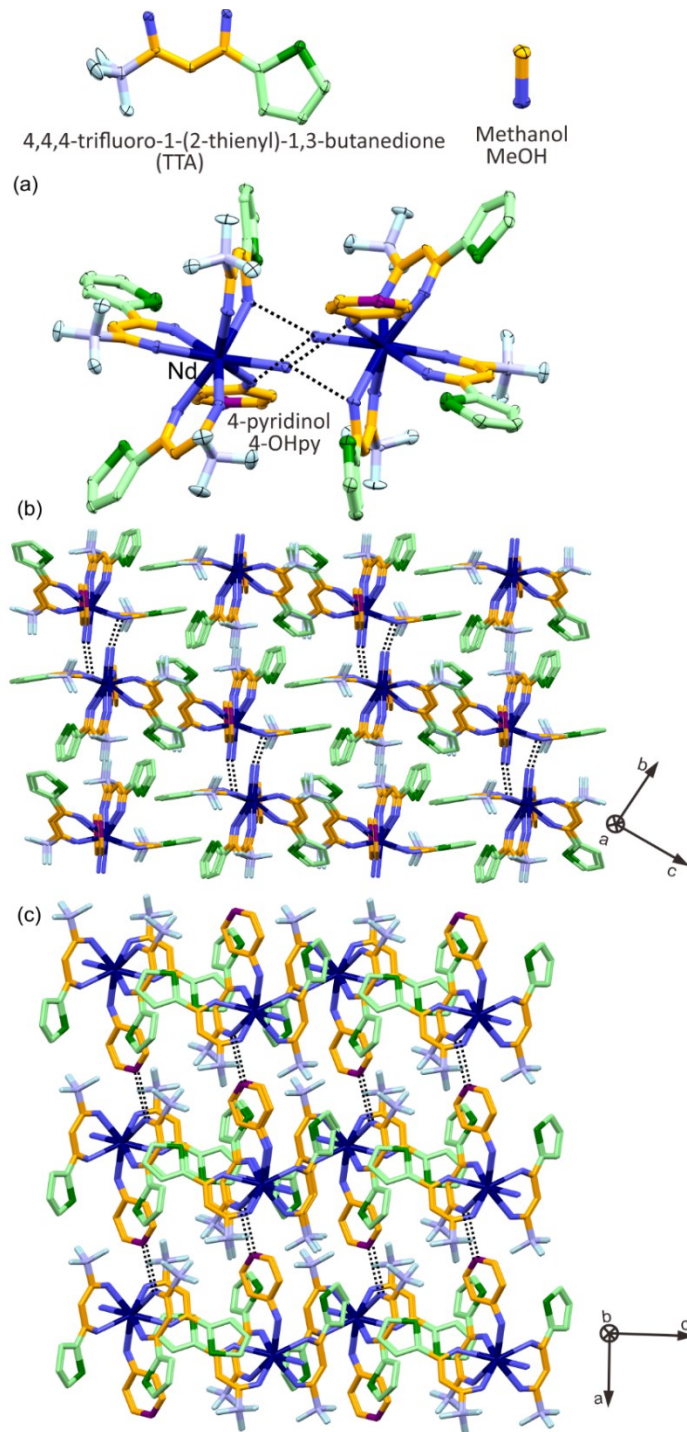


Figure S6. Detailed views of the crystal structure of **B**: (a) the single asymmetric unit connected with each other in dimeric fashion through hydrogen-bonding; (b) the view of supramolecular arrangement of **B** along tilted *a*-axis; (c) the view along tilted *b*-axis with indicated hydrogen bonding by black dotted lines.

Table S2. Detailed structural parameters of **A** and **B**.

	Parameter	A (Azo-py)	B (4-Cl) Parameter	Parameter	A (Azo-py)	B (4-Cl) Parameter
Bond lengths (Å)	Nd–O1	2.391(4)	2.437(2)	Nd–O5	2.398(4)	2.480(2)
	Nd–O2	2.406(4)	2.388(2)	Nd–O6	2.407(4)	2.392(2)
	Nd–O3	2.425(4)	2.428(2)	Nd–O7	2.487(4)	2.430(2)
	Nd–O4	2.408(3)	2.432(2)	Nd–O8	2.554(4)	2.488(2)
Angles (°)	O1–Nd–O2	70.78(14)	71.42(7)	O3–Nd–O4	71.41(13)	69.31(7)
	O1–Nd–O3	123.26(14)	140.69(7)	O3–Nd–O5	138.67(14)	114.98(8)
	O1–Nd–O4	75.07(14)	143.33(7)	O3–Nd–O6	139.79(14)	72.53(8)
	O1–Nd–O5	83.82(14)	75.44(7)	O3–Nd–O7	75.24(14)	75.83(7)
	O1–Nd–O6	76.94(14)	76.48(7)	O3–Nd–O8	136.54(13)	77.52(8)
	O1–Nd–O7	139.35(14)	78.40(7)	O4–Nd–O5	149.92(14)	139.43(9)
	O1–Nd–O8	139.99(14)	122.76(8)	O4–Nd–O6	83.23(14)	104.56(7)
	O2–Nd–O3	78.57(14)	146.15(7)	O4–Nd–O7	78.80(14)	138.09(7)
	O2–Nd–O4	109.02(14)	87.68(7)	O4–Nd–O8	136.36(13)	76.08(8)
	O2–Nd–O5	83.12(14)	77.65(7)	O5–Nd–O6	71.14(14)	70.66(7)
	O2–Nd–O6	140.49(14)	139.41(8)	O5–Nd–O7	105.50(14)	148.13(7)
	O2–Nd–O7	148.49(14)	110.73(8)	O5–Nd–O8	72.78(14)	136.03(7)
	O2–Nd–O8	74.50(14)	72.91(8)	O6–Nd–O7	69.47(14)	85.83(7)
				O6–Nd–O8	122.59(14)	147.32(8)
				O7–Nd–O8	79.23(14)	74.28(7)

Table S3. Results of Continuous Shape Measure (CSM) analyses for $[\text{Nd}^{\text{III}}(\text{TTA})_3(\text{CH}_3\text{OH})_2]$ structural units in the crystal structures of **A**.

Compound	CShM parameters*				Geometry
	SAPR-8	TDD-8	JBTPR-8	BTPR-8	
Ideal SAPR-8	0	2.848	2.843	2.267	
Ideal TDD-8	2.848	0	3.361	2.717	
Ideal JBTPR-8	2.843	3.361	0	1.439	
Ideal BTPR-8	2.267	2.717	1.439	0	
A (90 K)	0.924	1.862	2.396	1.944	SAPR-8
A (340 K)	0.940	2.141	2.514	2.082	SAPR-8

*CSM parameters: CSM SAPR-8 = the parameter related to the Square antiprism (D_{4d} symmetry); CSM TDD-8 = the parameter related to the Triangular dodecahedron (D_{2d} symmetry); CSM JBTPR-8 = the parameter related to the Biaugmented trigonal prism J50 (C_{2v} symmetry); CSM BTPR-8 = the parameter related to the Biaugmented trigonal prism (C_{2v} symmetry); CSM = 0 for the ideal geometry, and increases with the increasing distortion from the ideal polyhedron.⁵⁵

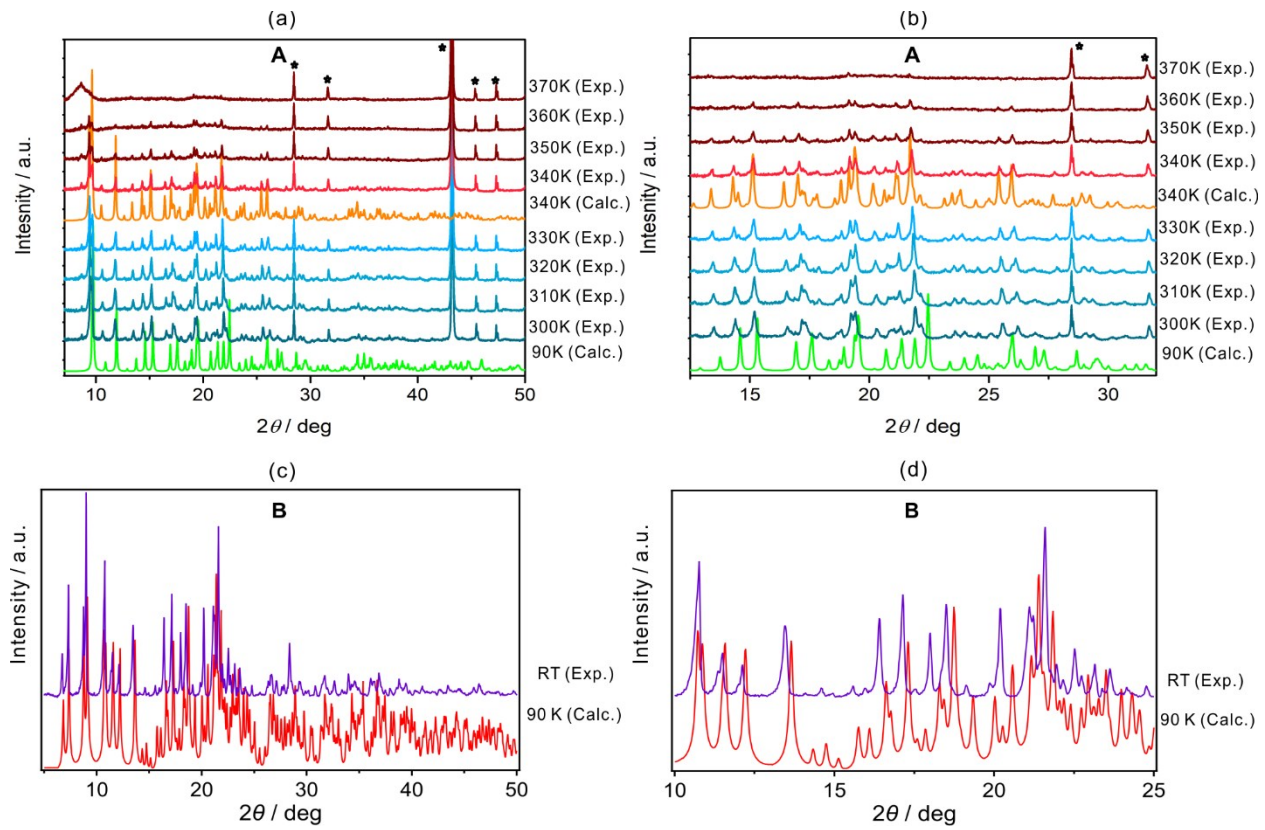


Figure S7. Experimental powder X–ray diffraction patterns of **A** and **B** compared with simulated ones for single crystal structures. Here, Exp. Indicates experimental and Calc. means calculated crystal structures. The black asterisk indicates the silicon peak which is used to correct the peak position.

Comment to powder X–ray diffraction patterns.

The systematic shift of measured diffraction patterns compared to simulated one originate in the temperature effect as the single–crystal X–ray diffraction measurements and the powder X–ray diffraction experiments were performed at different temperature. In order to confirm the chemical composition of compound after heating to 370 K, powdered samples were heated in TGA under similar condition to PXRD measurements and used for the CHNSF elemental analysis. Chemical composition after heating the sample removes 3/4th of methanol from the asymmetric unit – Anal. calcd. C, 38.56%; H, 2.3%; N, 3.05 %; F, 18.6%; S, 10.5%. Found: C, 38.4%; H, 2.5%; N, 2.9%; F, 18.6%; S, 10.35%. This also confirms that the physical properties observed after heating sample to 370 K originates from the complex **A** with less number of methanol compared to before heating complex.

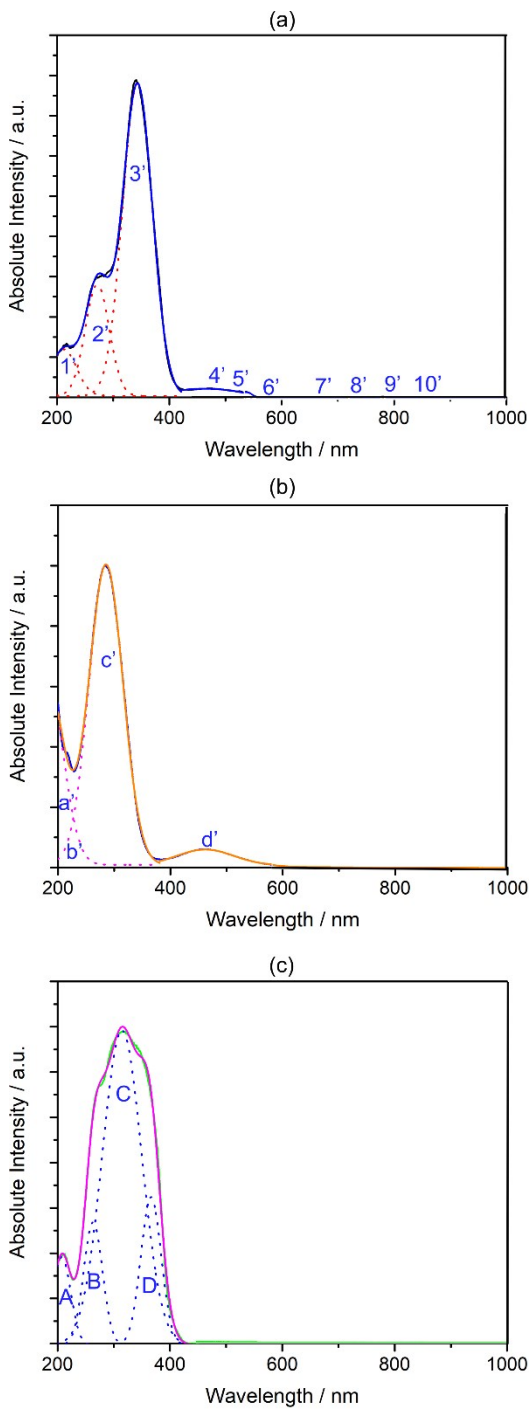


Figure S8. Room temperature solid-state UV–Vis–NIR absorption (Kubelka–Munk function) spectra of **A** (*a*) compared with relevant spectra of Azo-py (*b*) and TTA (*c*) in 200 – 1000 nm. The solid coloured lines are experimental data overlapped with fitted curve and dotted lines indicates the Gaussian deconvolution of the experimental spectra.

Table S4. Assignment of UV-Vis-NIR absorption spectra of A, Azo-py and TTA (**Figure S7**).

Compound	peak no.	λ_{\max} [nm]	Intensity maxima [a.u.]	Interpretation
A	1'	212	0.026	combined contributions from singlet to singlet transitions ($\pi \rightarrow \pi^*$) of Azo-py and TTA
	2'	272	0.06	combined contributions from singlet to singlet transitions ($\pi \rightarrow \pi^*$) of Azo-py and TTA
	3'	343	0.16	combined contributions from singlet to singlet transitions ($\pi \rightarrow \pi^*$) of Azo-py and TTA
	4'	463	0.004	Combined contribution of singlet to singlet transitions ($\pi \rightarrow \pi^*$) of Azo-py and f-f transition of Nd ^{III} : $^{5S} 4I_{9/2} \rightarrow ^2G_{9/2}, ^4G_{11/2}, ^2K_{15/2}$
	5'	525	0.003	Combined contribution of singlet to singlet transitions ($\pi \rightarrow \pi^*$) of Azo-py and f-f transition of Nd ^{III} : $4I_{9/2} \rightarrow ^4G_{7/2}, ^4G_{9/2}, ^2K_{13/2}$
	6'	582	0.003	f-f transition of Nd ^{III} : $4I_{9/2} \rightarrow ^2G_{7/2}, ^4G_{5/2}$
	7'	682	0.0001	f-f transition of Nd ^{III} : $4I_{9/2} \rightarrow ^4F_{9/2}$
	8'	746	0.0006	f-f transition of Nd ^{III} : $4I_{9/2} \rightarrow ^4S_{3/2}, ^4F_{7/2}$
	9'	803	0.0008	f-f transition of Nd ^{III} : $4I_{9/2} \rightarrow ^2H_{9/2}, ^4F_{5/2}$
	10'	878	0.00015	f-f transition of Nd ^{III} : $4I_{9/2} \rightarrow ^4F_{3/2}$
Azo-py	a'	216	0.38	singlet to singlet transitions ($\pi \rightarrow \pi^*$) ^{S6-S7}
	b'	285	1	
	c'	462	0.06	
TTA	A	207	0.29	singlet to singlet transitions ($\pi \rightarrow \pi^*$) ^{S8-10}
	B	263	0.73	
	C	315	1	
	D	366	0.76	singlet to singlet transitions (overlapping n \rightarrow π^* and $\pi \rightarrow \pi^*$ bands) ^{S8-10}

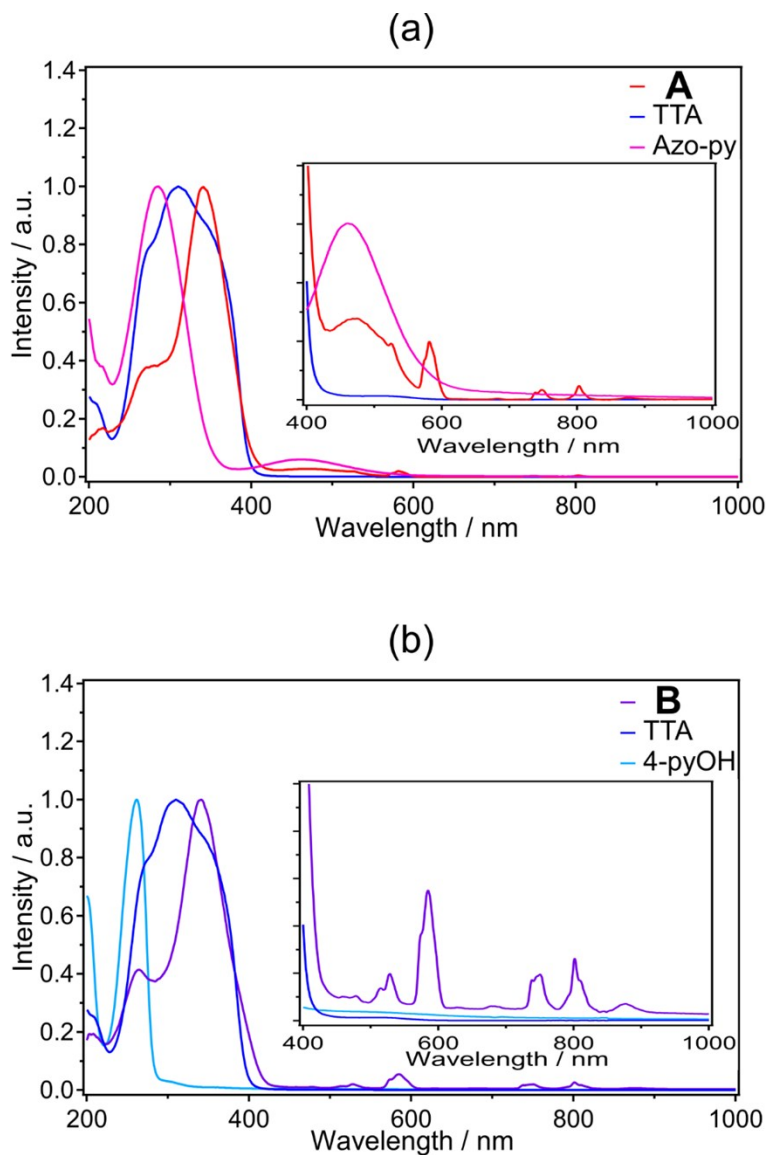


Figure S9. Room temperature solid-state UV-Vis-NIR absorption (Kubelka-Munk function) spectrum of **A** overlapped with spectra of Azo-py and TTA (*a*) as well as **B** overlapped with spectra of 4-pyOH and TTA (*b*) in 200 – 1000 nm wavelength range. Insets show zoomed the 400 – 1000 nm wavelength range corresponding to very weak Nd(III)-based absorption.

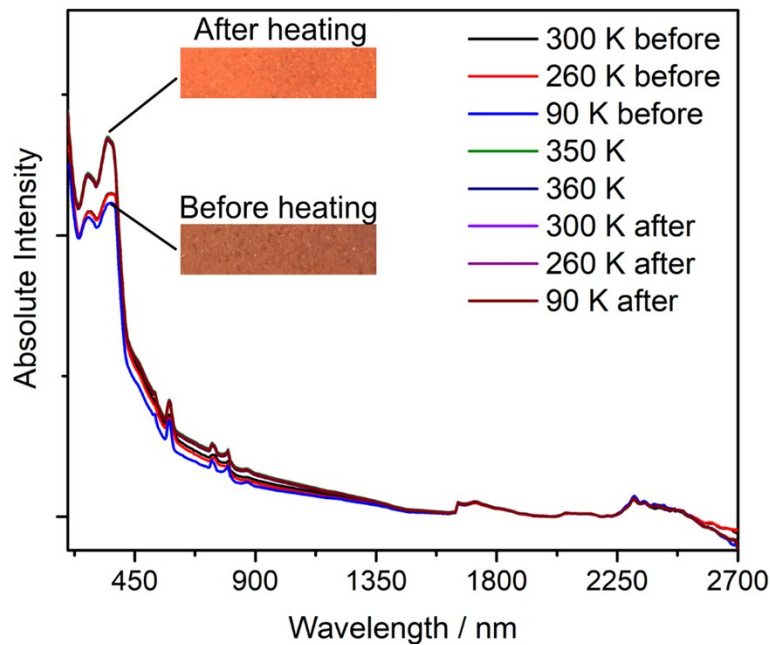


Figure S10. Temperature dependent UV–Vis–NIR absorption (Kubelka–Munk function) spectra of **A** in 200 – 2700 nm range.

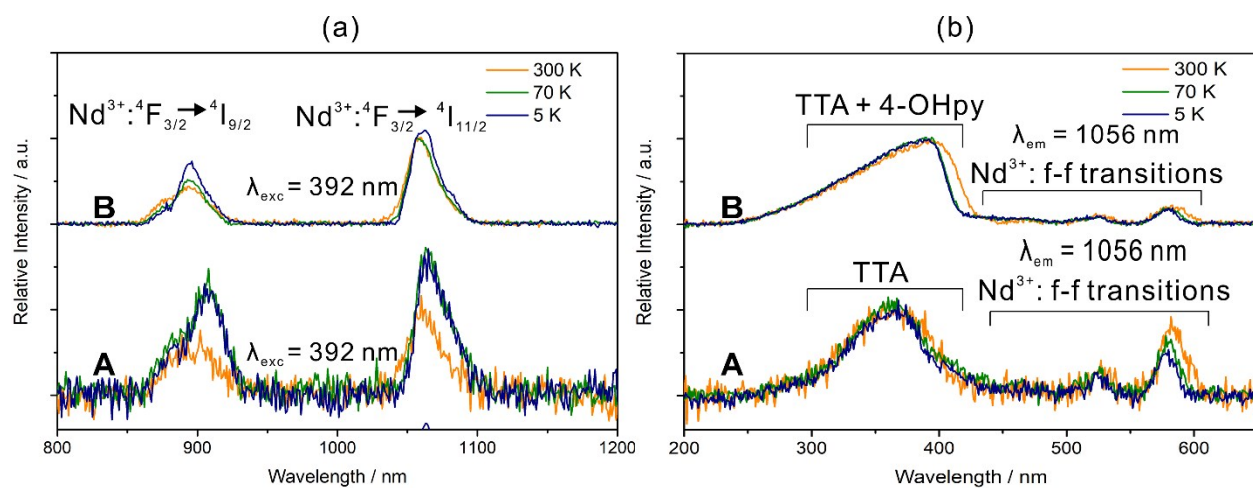


Figure S11. Comparison of emission and excitation spectra of **A** and **B** for the excitation wavelength of 392 nm at the indicated temperatures.

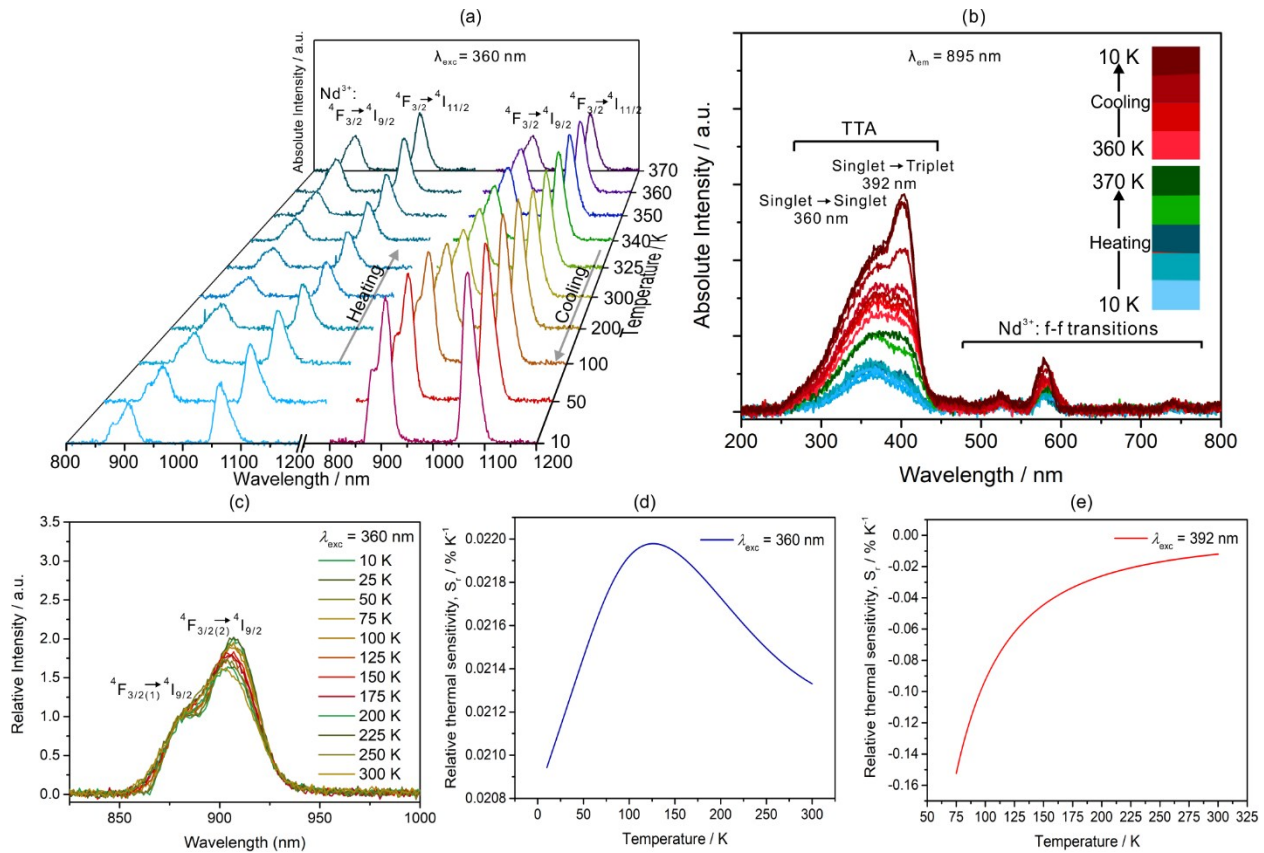


Figure S12. Solid state NIR emission measured for the temperature ranging from 10 - 370 K for the excitation wavelength of 360 nm in the heating and cooling cycle (a), the related excitation spectra of **A** measured at relevant emission wavelength of 895 nm (b) for shown temperatures and the emission peak at 895 nm measured at various temperature for excitation wavelength of 360 nm (c). Part (d) and (e) presents temperature dependences of relative thermal sensitivity, S_r , of compound **A** computed from the $\Delta(T)$ calibration curves for two investigated excitation wavelengths of 360 (Fig. 2) and 392 nm, respectively.

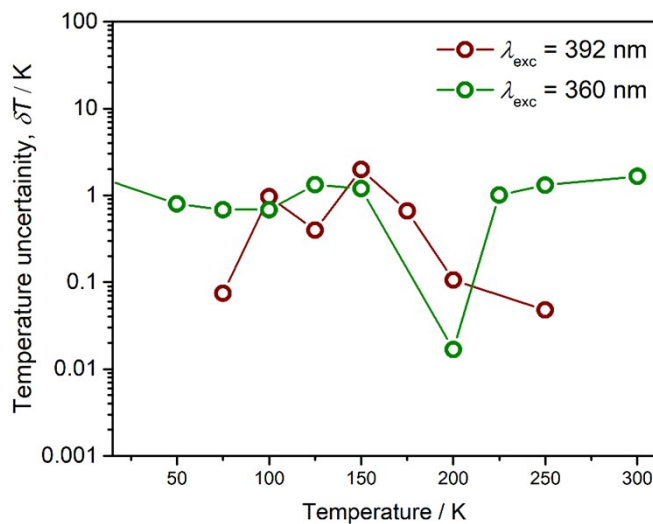


Figure S13. The temperature dependences of the temperature uncertainty, δT , calculated using the experimental relative errors of thermometric parameters, Δ for **A**.

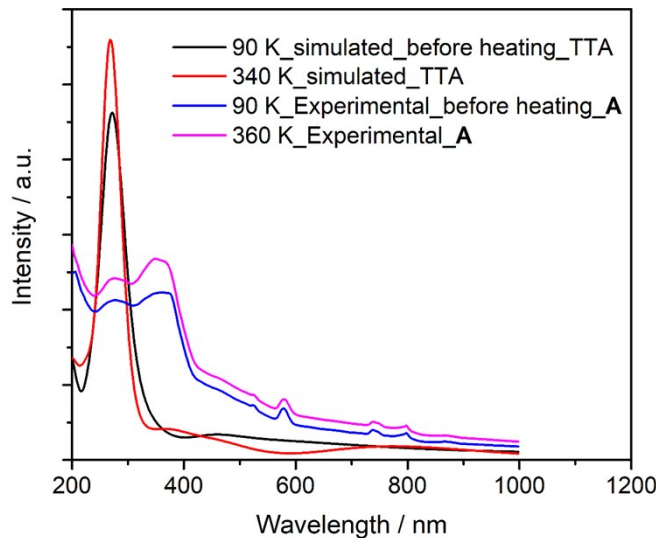


Figure S14. Stimulated UV–Vis–NIR absorption spectra of TTA and **A** in 200 – 1000 nm range using Gaussian 09 software and compared with experimental result.^{S2-S4}

Comments on UV-VIS-NIR absorption spectra.

Based on the structure model of TTA (figure 1c, manuscript) obtained from the XRD measurement, TD-DFT ((TD(NStates=100), B3LYP/6-31G(d,p)) calculation for excited states was performed by *Gaussian09* software to stimulate the UV-VIS spectra (computational detail, ESIT).^{S2-S3} The results indicated increased absorption intensity for the thermally-excited sample which is also confirmed by the experimental temperature dependent UV-VIS-NIR measurements (Fig. S9 and S12, ESIT).

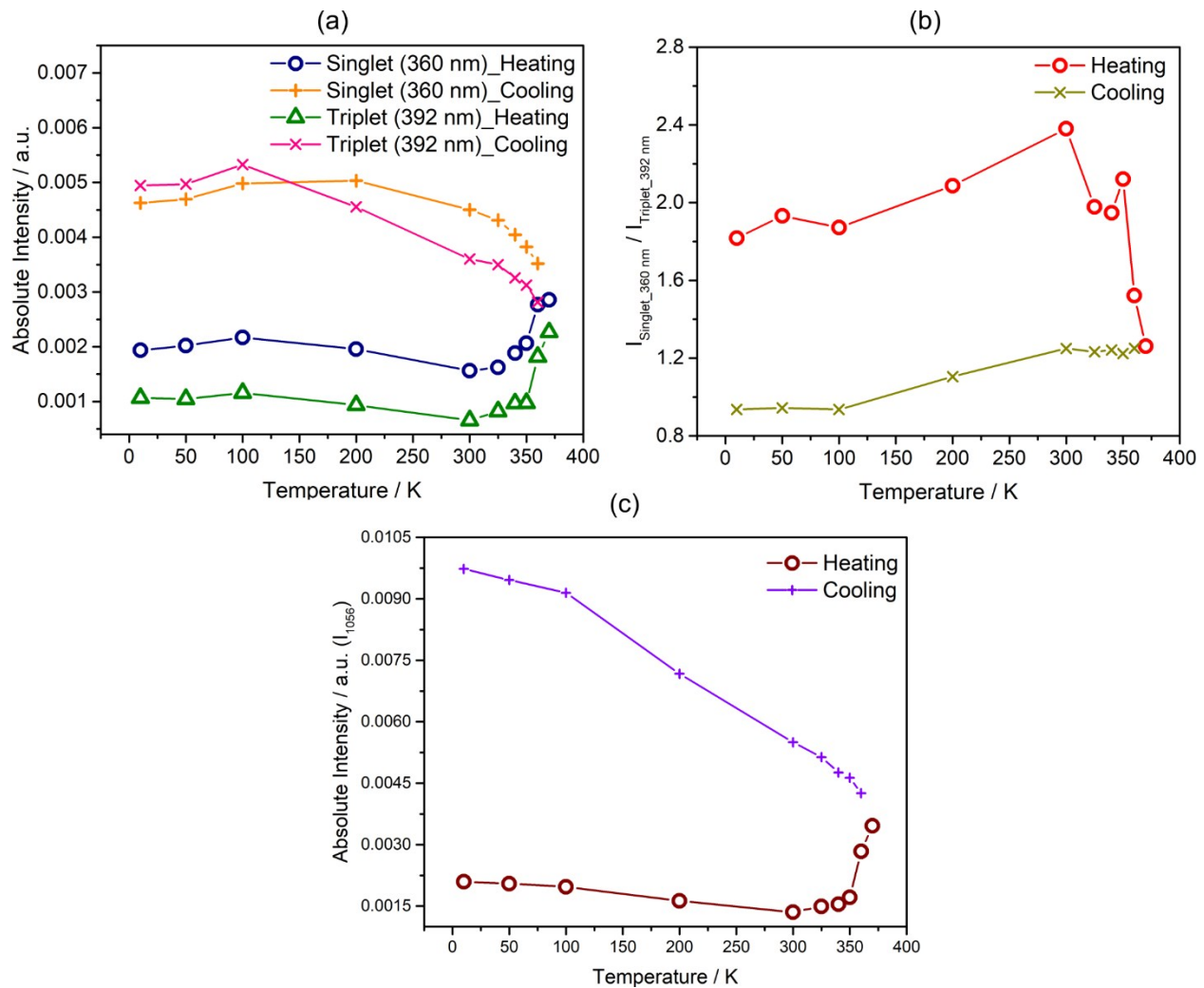


Figure S15. The temperature dependence of absolute intensity of the peak centred around 360 nm and 392 nm in the excitation spectra of **A** for the emission wavelength of 1056 nm (a), thermal dependent intensity ratio of corresponding peak at 360 and 392 nm in the excitation spectra of **A** and temperature dependence of absolute emission intensity peaked at 1056 nm for excitation light of 392 nm for complex **A**.

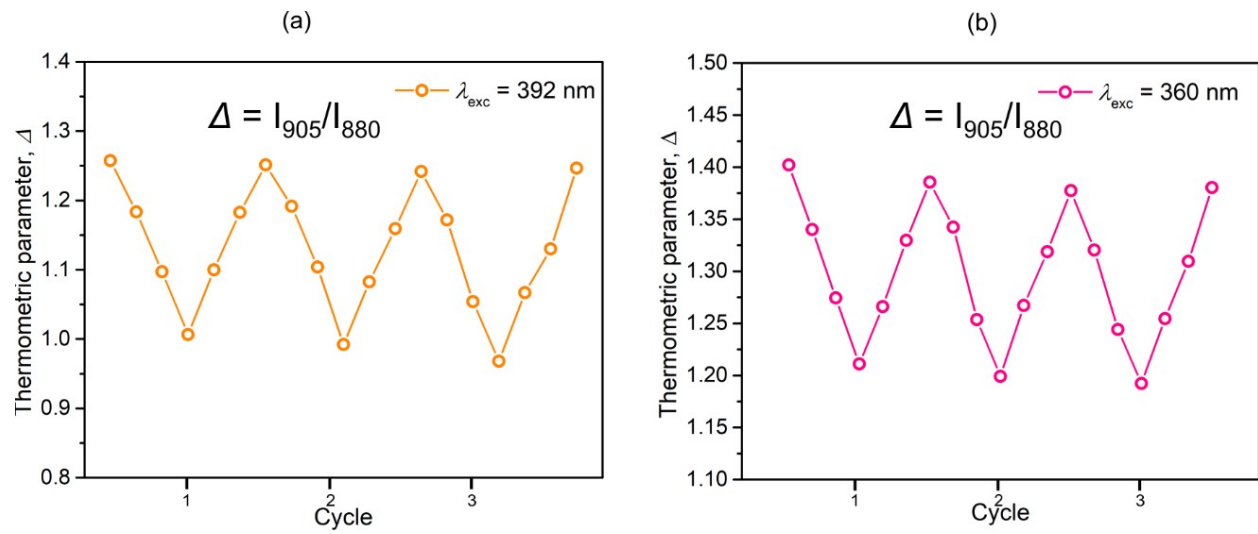


Figure S16. Trend of thermometric parameter, Δ for A under the excitation by 392 nm (a) and 360 nm (b) light during temperature cycling between 200 and 50 K showing nice repeatability for both excitation wavelengths.

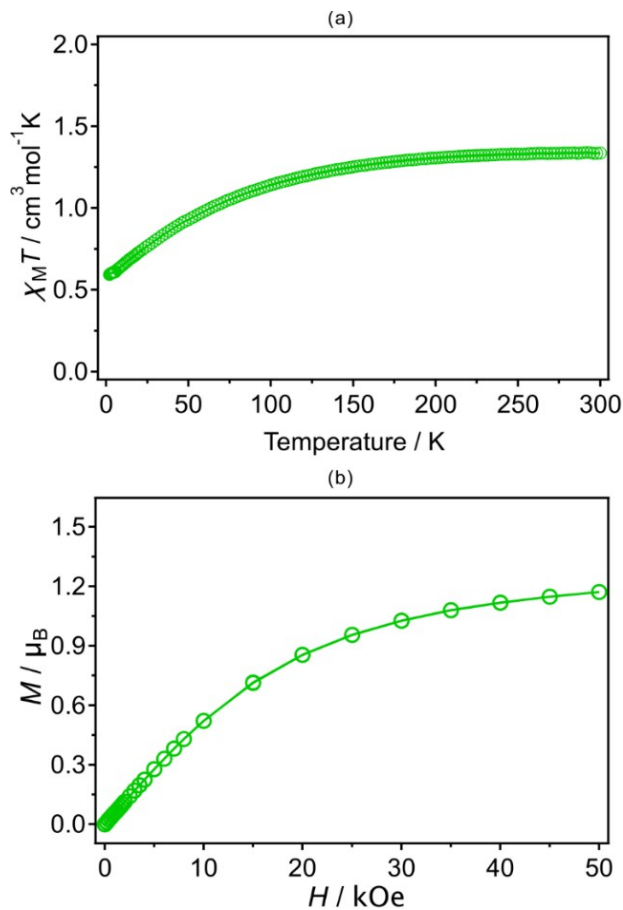


Figure S17. The *dc* magnetic properties: (a) temperature dependences of product molar magnetic susceptibility and temperature ($\chi_M T$) in $H_{dc} = 1 \text{ kOe}$ for **A** and (b) magnetic field dependences of magnetization at $T = 1.85 \text{ K}$ for **A**. Solid lines are presented only to guide the eye.

Debye model for single relaxation process

The following equations of the generalized Debye model for single relaxation process were applied:

$$\chi'(\omega) = \chi_S + (\chi_T - \chi_S) \frac{1 + (\omega\tau)^{1-\alpha} \sin(\pi\alpha/2)}{1 + 2(\omega\tau)^{1-\alpha} \sin(\pi\alpha/2) + (\omega\tau)^{2(1-\alpha)}} \quad (\text{E1})$$

$$\chi''(\omega) = (\chi_T - \chi_S) \frac{(\omega\tau)^{1-\alpha} \cos(\pi\alpha/2)}{1 + 2(\omega\tau)^{1-\alpha} \sin(\pi\alpha/2) + (\omega\tau)^{2(1-\alpha)}} \quad (\text{E2})$$

where: χ_S = the adiabatic susceptibility (at infinitely high frequency of *ac* field), χ_T = the isothermal susceptibility (at infinitely low frequency of *ac* field), τ = the relaxation time, α = the

distribution (Cole–Cole) parameter, and ω is an angular frequency, that is $\omega = 2\pi\nu$, with ν stands for the linear frequency in [Hz] units.^{S11}

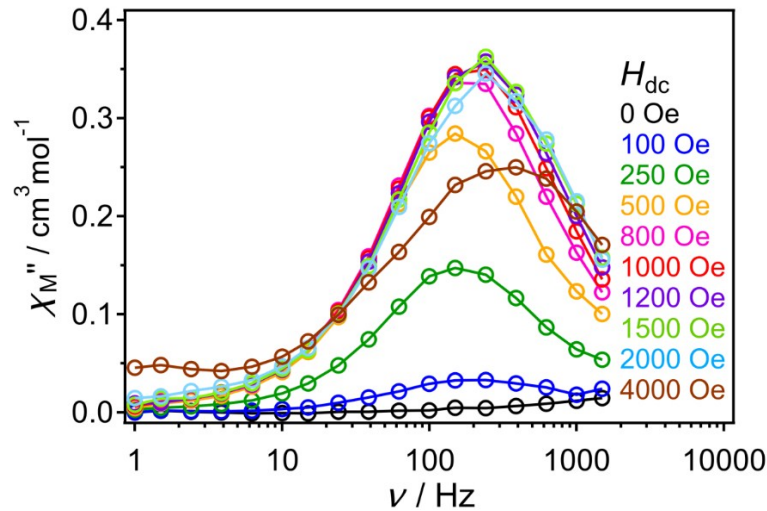


Figure S18. Frequency dependencies of out-of-plane χ_M'' magnetic susceptibility of **A** in *ac* magnetic field of 3 Oe at $T = 1.85$ K in various indicated *dc* magnetic fields. Solid lines are presented only to guide the eye.

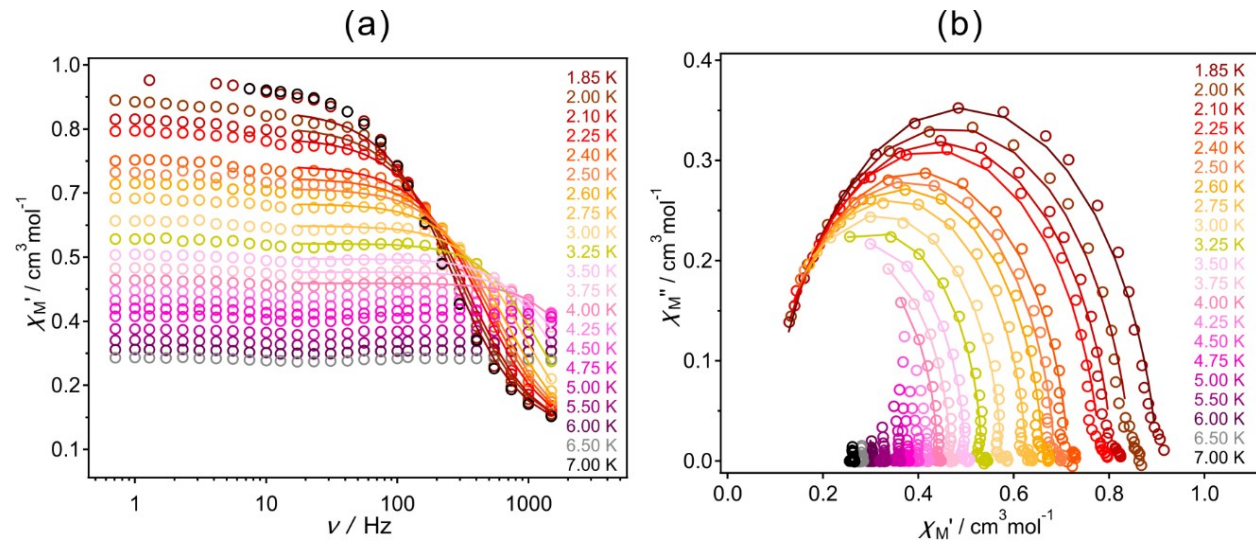


Figure S19. The *ac* magnetic characteristics of the **A** in $H_{dc} = 1000$ Oe and $H_{ac} = 3$ Oe: frequency (ν) dependences of the in-plane χ_M' (a) and the related $\chi_M'' - \chi_M'$ Argand plots (b). Solid lines were fitted using the generalized Debye model (Equation E1 and E2).

Table S5. Parameters obtained by fitting the Argand $\chi_M'' - \chi_M'$ plots ($H_{dc} = 1000$ Oe, Figure 9) of **A** using the generalized Debye model.

T / K	χ_s $\text{cm}^3\text{mol}^{-1}$	χ_T $\text{cm}^3\text{mol}^{-1}$	τ / s	α
1.85	$8.66 \cdot 10^{-2}$	0.901	$7.43 \cdot 10^{-4}$	$9.20 \cdot 10^{-2}$
2.00	$8.14 \cdot 10^{-2}$	0.847	$6.12 \cdot 10^{-4}$	$8.79 \cdot 10^{-2}$
2.10	$8.20 \cdot 10^{-2}$	0.807	$5.31 \cdot 10^{-4}$	$8.21 \cdot 10^{-2}$
2.25	$7.59 \cdot 10^{-2}$	0.782	$4.74 \cdot 10^{-4}$	$8.17 \cdot 10^{-2}$
2.40	$7.68 \cdot 10^{-2}$	0.715	$3.66 \cdot 10^{-4}$	$6.32 \cdot 10^{-2}$
2.50	$7.34 \cdot 10^{-2}$	0.686	$3.20 \cdot 10^{-4}$	$5.84 \cdot 10^{-2}$
2.60	$7.56 \cdot 10^{-2}$	0.661	$2.85 \cdot 10^{-4}$	$4.72 \cdot 10^{-2}$
2.75	$6.89 \cdot 10^{-2}$	0.626	$2.35 \cdot 10^{-4}$	$4.06 \cdot 10^{-2}$
3.00	$6.68 \cdot 10^{-2}$	0.573	$1.76 \cdot 10^{-4}$	$1.92 \cdot 10^{-2}$
3.25	$7.26 \cdot 10^{-2}$	0.532	$1.35 \cdot 10^{-4}$	$1.56 \cdot 10^{-4}$
3.50	$5.80 \cdot 10^{-2}$	0.496	$9.79 \cdot 10^{-5}$	$2.31 \cdot 10^{-4}$
3.75	$4.83 \cdot 10^{-2}$	0.465	$7.22 \cdot 10^{-5}$	$3.80 \cdot 10^{-4}$
4.00	$1.75 \cdot 10^{-2}$	0.439	$5.02 \cdot 10^{-5}$	$5.75 \cdot 10^{-4}$
4.25	$8.88 \cdot 10^{-8}$	0.414	$3.64 \cdot 10^{-5}$	$4.44 \cdot 10^{-4}$

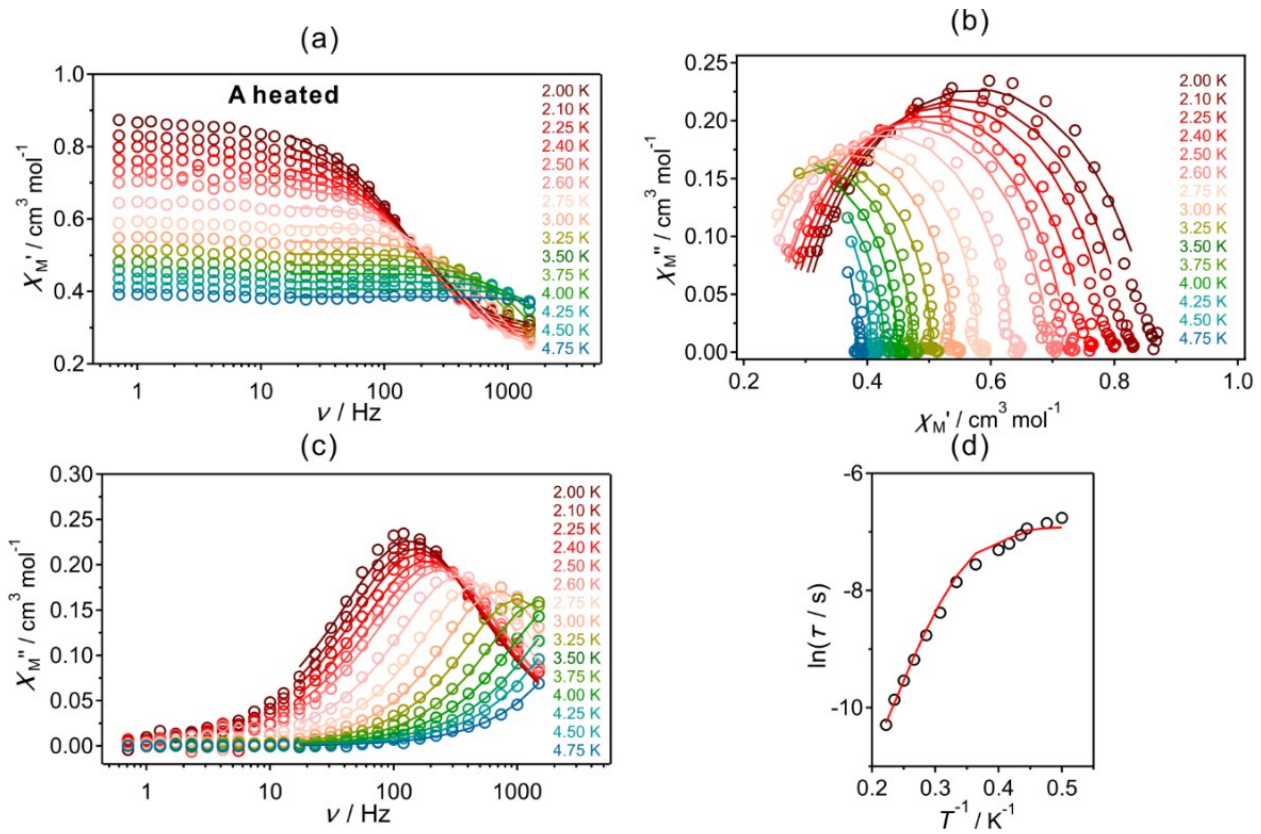


Figure S20. The *ac* magnetic characteristics of sample **A** after heating at 360 K in $H_{dc} = 1000$ Oe and $H_{ac} = 3$ Oe: frequency (ν) dependences of the in-plane χ_M' (a) and the related $\chi_M''-\chi_M'$ Argand plots (b), frequency (ν) dependences out-of-plane, χ_M'' (c) components of the complex magnetic susceptibility for the indicated temperatures of the 1.85–7.0 K range and the temperature dependence of relaxation times (τ) presented as $\ln(\tau)$ versus T^{-1} plots (d). Solid lines in (a), (b), (c) were fitted using the generalized Debye model, whereas the solid line in (d) are fitted with Arrhenius law, Orbach and the quantum tunnelling of the magnetization (QTM) (Equation E1 and E2).

Table S6. The outline of Nd^{III} complexes revealing single-molecule magnet behaviour.

compound	$\Delta E/k_B$ / K	τ_0 / s	H_{dc} / Oe	Ref.
A	19.7(7)	$3.7(8)\cdot 10^{-7}$	1000	this work
A heated	27.3(1)	$8.5(0)\cdot 10^{-8}$	1000	this work
zero-dimensional molecular systems				
[Li(dme) ₃][Nd ^{III} (COT'') ₂] (dme = dimethoxyethane; COT'' = bis(trimethylsilyl)cyclooctatetraenyl dianion)	21	$5.5\cdot 10^{-5}$	1000	S12
[Nd ^{III} (Tp) ₃] (Tp = trispyrazolylborate)	4.1(1)	$4.2(2)\cdot 10^{-5}$	100	S13
[Nd ^{III} (^t BuPO(NH ⁱ Pr) ₂) ₂ (H ₂ O) ₅]I ₃ ·H ₂ O	24.69 16.08 39.21	$5.03\cdot 10^{-6}$ $2.64\cdot 10^{-6}$ $8.98\cdot 10^{-6}$	0 0 2000	S14
Na ₉ [Nd ^{III} (W ₅ O ₁₈) ₂]	73.9	$3.55\cdot 10^{-10}$	1000	S15
[Nd ^{III} (NO ₃) ₃ (18-crown-6)]	33.4(5)	$1.6(2)\cdot 10^{-9}$	1000	S16
[Nd ^{III} (NO ₃) ₃ (1,10-diaza-18-crown-6)]	73(2)	$1.4(6)\cdot 10^{-10}$	1000	S17
(NH ₂ Me ₂) ₃ {[Nd ^{III} (Mo ₄ O ₁₃)(dmf) ₄] ₃ (btc) ₂ }·8(dmf) (btc = 1,3,5-benzentricarboxylate anion)	34.06	$4.69\cdot 10^{-8}$	500	S18
[Nd ^{III} (Cp*) ₂](BPh ₄) (Cp* = pentamethylcyclopentadienyl anion)	41(2)	$1.4(4)\cdot 10^{-6}$	1000	S19
one-dimensional coordination polymers				
[Nd ^{III} ₂ (CNCH ₂ COO) ₆ (H ₂ O) ₄]<·2H ₂ O	26.6(1)	$1.75\cdot 10^{-7}$	1500	S20
{[Nd ^{III} (pzdo)(H ₂ O) ₄][Co ^{III} (CN) ₆]}·0.5(pzdo)·4H ₂ O	51(2)	$4.5(9)\cdot 10^{-8}$	1000	S21
[Nd ^{III} (3,5-dnb) ₃ (H ₂ O) ₂]·MeCN (3,5-dnb = 3,5-dinitrobenzoic acid anion)	27	$4.1\cdot 10^{-7}$	2000	S22
[Nd ^{III} (2,4-dnb) ₂ (CH ₃ COO)(H ₂ O) ₂] (2,4-dnb = 2,4-dinitrobenzoic acid anion)	29	$3.1\cdot 10^{-7}$	3500	S23

References to Supporting Information

- [S1] G. Boehm and M. Dwyer, *J. Chem. Educ.*, 1981, **58**, 809.
- [S2] M. J. Frisch, G. W. Trucks, H. B. Schlegel, G. E. Scuseria, M. A. Robb, J. R. Cheeseman, G. Scalmani, V. Barone, B. Mennucci, G. A. Petersson, H. Nakatsuji, M. Caricato, X. Li, H. P. Hratchian, A. F. Izmaylov, J. Bloino, G. Zheng, J. L. Sonnenberg, M. Hada, M. Ehara, K. Toyota, R. Fukuda, J. Hasegawa, M. Ishida, T. Nakajima, Y. Honda, O. Kitao, H. Nakai, T. Vreven, J. A. Montgomery Jr, J. E. Peralta, F. Ogliaro, M. Bearpark, J. J. Heyd, E. Brothers, K. N. Kudin, V. N. Staroverov, T. Keith, R. Kobayashi, J. Normand, K. Raghavachari, A. Rendell, J. C. Burant, S. S. Iyengar, J. Tomasi, M. Cossi, N. Rega, J. M. Millam, M. Klene, J. E. Knox, J. B. Cross, V. Bakken, C. Adamo, J. Jaramillo, R. Gomperts, R. E. Stratmann, O. Yazyev, A. J. Austin, R. Cammi, C. Pomelli, J. W. Ochterski, R. L. Martin, K. Morokuma, V. G. Zakrzewski, G. A. Voth, P. Salvador, J. J. Dannenberg, S. Dapprich, A. D. Daniels, Ö. Farkas, J. B. Foresman, J. V. Ortiz, J. Cioslowski and D. J. Fox, *Gaussian 09*, Revision C.01, Gaussian, Inc., Wallingford CT, 2010.
- [S3] A. D. Becke, *J. Chem. Phys.*, 1993, **98**, 5648.
- [S4] M. Llunell, D. Casanova, J. Cirera, J. Bofill, P. Alemany, S. Alvarez, M. Pinsky and D. Avnir, *SHAPE v. 2.1. Program for the Calculation of Continuous Shape Measures of Polygonal and Polyhedral Molecular Fragments*, University of Barcelona: Barcelona, Spain, 2013.
- [S5] S. Chorazy, T. Charytanowicz, J. Wang, S. Ohkoshi and B. Sieklucka, *Dalton Trans.*, 2018, **47**, 7870.
- [S6] J. P. Launay, M. Tourrel-Pagois, J. F. Lipskier, V. Marvaud, C. Joachim, *Inorg. Chem.*, 1991, **30**, 1033.
- [S7] J. Otsuki, N. Omokawa, K. Yoshioka, I. Yoshikawa, T. Akasaka, T. Suenobu, T. Takido, K. Araki, S. Fukuzumi, *Inorg. Chem.*, 2003, **42**, 3057.
- [S8] V. V. Khistiaeva, A. S. Melnikov, S. O. Slavova, V. V. Sizov, G. L. Starova, I. O. Koshevoy and E. V. Grachova, *Inorg. Chem. Front.*, 2018, **5**, 3015.
- [S9] K. S. Kisel, G. Linti, G. L. Starova, V. V. Sizov, A. S. Melnikov, A. P. Pushkarev, M. N. Bochkarev, E. V. Grachova and S. P. Tunik, *Eur. J. Inorg. Chem.*, 2015, **10**, 1734.
- [S10] N. Dannenbauer, P. R. Matthes, T. P. Scheller, Jörn Nitsch, S. H. Zottnick, M. S. Gernert, A. Steffen, C. Lambert, K. Müller-Buschbaum, *Inorganic Chemistry*, 2016, **55**, 7396.

- [S11] Y.-N. Guo, G.-F. Xu, Y. Guo and J. Tang, *Dalton Trans.*, 2011, **40**, 9953.
- [S12] J. J. Le Roy, S. I. Gorelsky, I. Korobkov and M. Murugesu, *Organometallics*, 2015, **34**, 1415.
- [S13] J. D. Rinehart and J. R. Long, *Dalton Trans.*, 2012, **41**, 13572.
- [S14] S. K. Gupta, T. Rajeshkumar, G. Rajaraman and R. Murugavel, *Chem. Commun.*, 2016, **52**, 7168.
- [S15] J. J. Baldovi, J. M. Clemente-Juan, E. Coronado, Y. Duan, A. Gaita-Arino and C. Gimenez-Saiz, *Inorg. Chem.*, 2014, **53**, 9976.
- [S16] H. Wada, S. Ooka, T. Yamamura and T. Kajiwara, *Inorg. Chem.*, 2017, **56**, 147.
- [S17] H. Zhang, X. Wu, J. Liao, X. Kuang, W. Yang and C. Lu, *Dalton Trans.*, 2018, **47**, 1796.
- [S18] S. Demir, K. R. Meihaus and J. R. Long, *J. Organomet. Chem.*, 2017, **857**, 164.
- [S19] A. Arauzo, A. Lazarescu, S. Shova, E. Bartolome, R. Cases, J. Luzon, J. Bartolome and C. Turta, *Dalton Trans.*, 2014, **43**, 12342.
- [S20] S. Chorazy, T. Charytanowicz, J. Wang, S. Ohkoshi and B. Sieklucka, *Dalton Trans.*, 2018, **47**, 7870.
- [S21] A. K. Jassal, N. Aliaga-Alcalde, M. Corbella, D. Aravena, E. Ruiz and G. Hundal, *Dalton Trans.*, 2015, **44**, 15774.